Entropy-bounded discontinuous-Galerkin simulation of trans- and supercritical fluid flows

By K. Maeda AND M. Ihme

1. Motivation and objectives

Trans- and supercritical fluid flows are of critical importance in industrial applications ranging from power generation, internal combustion engines, and rocket propulsion to low-temperature processing and manufacturing of chemical, pharmaceutical, and biomedical substances, as well as sub-surface energy storage and extraction (Knez *et al.* 2014). In supercritical states, the gas-liquid phase interface disappears and the fluid presents unique physical properties, such as gas-like high diffusivity and liquid-like high density. During pseudo-boiling (pseudo liquid-vapor phase change), which is the transition of a state from sub-critical to supercritical temperature at supercritical pressure, the fluid experiences a smooth change with a sharp gradient in density and a peak in heat capacity (Banuti *et al.* 2017). The consideration of such non-trivial properties and phenomena is critical for quantifying mixing and energy transport in fluids for these applications. Nevertheless, the detailed hydrodynamics of trans- and supercritical fluids have been relatively unexplored compared to their sub-critical counterparts. Experiments are limited in supercritical conditions; thus, high-fidelity simulation is desirable for understanding the flows.

Challenges in simulation of trans- and supercritical fluid flows involve implementation of models of real–fluid thermodynamics into an established framework for compressible flows of an ideal fluid with a constant heat capacity (hereafter we denote as calorically perfect fluid). Major previous approaches employed cubic equations of state for the thermodynamic modeling, and combined it with either finite-difference (FD) or finite-volume (FV) framework for the compressible Navier-Stokes equations (e.g., Miller *et al.* 2001; Terashima & Koshi 2012; Kawai *et al.* 2015; Ma *et al.* 2017; Pantano *et al.* 2017; Kim *et al.* 2019). Unlike calorically perfect fluid, real fluid possesses non-constant and state-dependent specific heat ratio, which can be a source of numerical instabilities that are otherwise not present (Billet & Abgrall 2003). In order to suppress instabilities in high-order methods, the aforementioned approaches employed techniques that are specialized for supercritical fluids, including double-flux formulation, non-conservative forms of equations, and *a priori* grid refinement. In exchange of robustness, such techniques may impose additional computational complexity and cost, and numerical artifacts that may overshadow favorable properties of the original framework including, for instance, discrete conservation, optimal dissipation and dispersion, and parallel efficiency.

Another existing numerical framework for a compressible flow is the high-order discontinuous-Galerkin (DG) method (e.g., Cockburn & Shu 1998; Fidkowski 2004; Mengaldo 2015). The DG method discretizes a domain into finite elements, each of which contains sub-element nodes. The sub-element flow field is treated as continuous and approximated by a set of orthogonal basis functions through a Galerkin projection. The flow field across the elements are treated as discontinuous and inter-element flux is obtained through the solution of a Riemann problem. Advantages of the DG method over

high-order FD and FV methods include its flexibility in grid structures and high parallel efficiency; arbitrary shapes of elements can be used for spatial discretization, which allows modeling of complex geometries. The method uses compact stencils for discretization, which minimizes the size of the buffer transferred between processors during MPI (message passing interface) communications. Previous efforts have been devoted to improving the robustness of the method while maintaining high-order accuracy by introducing techniques including limiters (de Frahan *et al.* 2015; Shu 2016), entropy-bounding strategies (Lv & Ihme 2015), and artificial viscosity (AV) (Persson & Peraire 2006; Lv *et al.* 2016; Ching *et al.* 2019). Aside from a recent contribution (Föll *et al.* 2019), application of the DG framework to simulations of trans- and supercritical fluid flows has largely been unexplored.

In this work, we develop a method for simulation of trans- and supercritical fluid flows using a high-order DG method. In order to fully take advantage of the favorable properties of DG methods, we aim to generalize the framework without interfering with the discrete conservation properties, high-order accuracy, and parallel efficiency. From this perspective, we focus on the following aspects: adoption of an approximate Riemann solver that was developed for simulation of non-ideal gas dynamics in the FV framework (Guardone 2007; Maeda *et al.* 2014) and extension of a DG method that employs an entropy-bounding technique for stabilization of shock capturing in calorically perfect gas (Lv & Ihme 2015). The rest of the paper is organized as follows: In Section 2, we present the formulation and numerical discretization. In Section 3, for validation and demonstration purposes, we simulate problems of a transcritical density wave, transcritical shock tube, and density stratified shear layers of trans- and supercritical nitrogen. The Peng-Robinson equation of state (Robinson *et al.* 1985) is used in these simulations. In Section 4, we state conclusions.

2. Formulation

2.1. *Equations of motion*

We formulate the dynamics of single-component, transcritical fluid flows using the compressible Navier-Stokes equation

$$\frac{\partial \rho}{\partial t} + \nabla \cdot (\rho \boldsymbol{u}) = 0, \tag{2.1}$$

$$\frac{\partial (\rho \boldsymbol{u})}{\partial t} + \nabla \cdot (\rho \boldsymbol{u}\boldsymbol{u} + p\mathcal{I}) = \nabla \cdot \boldsymbol{\tau}, \tag{2.2}$$

$$\frac{\partial E^t}{\partial t} + \nabla \cdot ((E^t + p)\boldsymbol{u}) = \nabla \cdot (\boldsymbol{u} \cdot \boldsymbol{\tau} - \boldsymbol{q}), \tag{2.3}$$

where ρ, $\boldsymbol{u}$, p, and E^t are the density, velocity, pressure, and total energy, respectively. $\boldsymbol{\tau}$ and $\boldsymbol{q}$ are the viscous stress tensor and the heat flux, respectively, defined as

$$\boldsymbol{\tau} = 2\mu(\mathcal{S} - \frac{1}{3}(\nabla \cdot \boldsymbol{u})\mathcal{I}), \tag{2.4}$$

$$\boldsymbol{q} = -\kappa \nabla T, \tag{2.5}$$

where $\mathcal{S}$ is the deformation rate tensor

$$\mathcal{S} = \frac{1}{2}(\nabla \boldsymbol{u} + \nabla \boldsymbol{u}^{\mathcal{T}}), \tag{2.6}$$

and T, μ, and κ are the temperature, viscosity, and the thermal conductivity, respectively.

The set of equations is closed with an equation of state

$$p = p(\rho, E), \tag{2.7}$$

where E is the total internal energy: $E = E^t - \rho \boldsymbol{u}^2/2$. In this study we present simulations using the Peng-Robinson equation of state, but the form is left general here for brevity.

2.2. *Discontinuous-Galerkin discretization*

We discretize the governing equation following the DG framework. For convenience, we express equations (2.1-2.3) in a vector form:

$$\frac{\partial \boldsymbol{U}}{\partial t} + \nabla \cdot \boldsymbol{F} = \nabla \cdot \boldsymbol{Q}. \tag{2.8}$$

The computational domain Ω is partitioned into a set of N_e non-overlapping elements $\Omega_e : e \in [1, ..., N_e]$, with boundaries $\partial\Omega_e$. The finite-dimensional test space V_p^h is defined as

$$V_h^p = \phi \in L^2(\Omega), \phi^e \equiv \phi|_{\Omega_e} \in P_p(\Omega_e)^{\forall}\Omega_e \in \Omega, \tag{2.9}$$

where ϕ is the test function and P_p denotes the space spanned by polynomial functions of degree p. The global solution $\boldsymbol{U}$ is approximated by $\boldsymbol{U} = \oplus_{e=1}^{N_e} \boldsymbol{U}^e$, using the local polynomial projection given by

$$\boldsymbol{U}_e(\boldsymbol{x}, t) = \sum_{n=1}^{N_p} \tilde{\boldsymbol{U}}_n^e(t) \phi_n^e(\boldsymbol{x}), \tag{2.10}$$

where $\tilde{\boldsymbol{U}}_n^e(t)$ is the n-th expansion coefficient, N_p is the number of polynomial coefficients, and ϕ_n is the polynomial basis function. In this work, we use Lagrange polynomials for the basis. By applying an integral operator $\int_{\Omega_e} \phi_m^e d\Omega_e$ to both sides of Eq. (2.8), we obtain a weak form of the governing equation

$$\int_{\Omega_e} \phi_m^e \frac{\partial \boldsymbol{U}^e}{\partial t} d\Omega_e + \int_{\Omega_e} \phi_m^e \nabla \cdot \boldsymbol{F} d\Omega_e = \int_{\Omega_e} \phi_m^e \nabla \cdot \boldsymbol{Q} d\Omega_e. \tag{2.11}$$

The left-hand side is approximated using orthogonality of the basis function and integration by parts as

$$\int_{\Omega_e} \phi_m^e \frac{\partial \boldsymbol{U}^e}{\partial t} d\Omega_e + \int_{\Omega_e} \phi_m^e \nabla \cdot \boldsymbol{F} d\Omega_e \tag{2.12}$$

$$\approx \sum_{n=1}^{N_p} d_t \tilde{\boldsymbol{U}}_n^e \int_{\Omega_e} \phi_m^e \phi_n^e d\Omega_e - \int_{\Omega_e} \nabla \phi_m^e \cdot \boldsymbol{F} d\Omega_e + \int_{\partial\Omega_e} \phi_m^{e+} \hat{\boldsymbol{F}} \cdot \hat{\boldsymbol{n}} d\Gamma_e, \tag{2.13}$$

where $\hat{\boldsymbol{n}}$ is the outward-pointing normal on $\partial\Omega_e$, and the superscripts $(\cdot)^+$ and $(\cdot)^-$ denote the interior and exterior of element Ω_e, respectively. The interior numerical flux $\boldsymbol{F}$ is directly computed as a function of $\boldsymbol{U}$ in each element, while the inter-element numerical flux $\hat{\boldsymbol{F}}$ is evaluated using a Riemann solver.

We linearize the diffusion flux such that in terms of ith state variable

$$\boldsymbol{Q}_i = \sum_{k=1}^{N_U} \mathcal{D}_{ik} \cdot \nabla U_k, \tag{2.14}$$

where $\mathcal{D}$ is the differentiation of the diffusive flux with respect to the gradient of the

state: $\mathcal{D} = \partial \boldsymbol{Q}/\partial(\nabla \boldsymbol{U})$. The right-hand side of equation (2.11) is expressed as

$$\int_{\Omega_e} \phi_m^e \nabla \cdot \boldsymbol{Q}_i d\Omega_e = \sum_{k=1}^{N_U} \int_{\Omega_e} \phi_m^e \nabla \cdot \boldsymbol{Q}_i^k d\Omega_e, \tag{2.15}$$

where the integral is approximated as

$$\begin{aligned}\int_{\Omega_e} \phi_m^e \nabla \cdot \boldsymbol{Q}_i^k d\Omega_e \approx &- \int_{\Omega_e} \nabla \phi_m^e \cdot (\mathcal{D}_{ik} \cdot \nabla \boldsymbol{U}_k) d\Omega_e \\ &+ \int_{\partial\Omega_e} (\boldsymbol{U}_k^+ - \hat{\boldsymbol{U}}_k)(\mathcal{D}_{ik}^T \cdot \nabla \phi_m^e)^+ \cdot \boldsymbol{n} d\Gamma_e + \int_{\partial\Omega_e} \phi_m^{e+} \hat{\boldsymbol{Q}}_i^k d\Gamma_e.\end{aligned} \tag{2.16}$$

Integrals in Eqs. (2.13) and (2.16) are evaluated using a Gaussian quadrature rule with an accuracy of $2p+1$.

The critical difference between the present method and the DG method for ideal gases is in the procedure to obtain the numerical fluxes $\boldsymbol{F}$ and $\hat{\boldsymbol{F}}$ and the gradient $\mathcal{D}$ from the given state $\boldsymbol{U}$. Details are addressed in the next section.

2.3. *Flux computation in the real fluid*

In the conservative form of the Euler and Navier-Stokes equations, the inviscid flux is expressed as a function of the conservative state variables: $\boldsymbol{F} = \boldsymbol{F}(\boldsymbol{U})$. the density and internal energy are only thermodynamic variables which are directly available from the state variables: $\rho = U_1$ and $E = U_3 - \boldsymbol{U}_2^2/2U_1$, where we express $\boldsymbol{U}$ as $\boldsymbol{U} = [U_1, \boldsymbol{U}_2^T, U_3]^T$. Meanwhile, the momentum flux includes pressure, which is a primitive variable. In general, an equation of state is used as a closure to express pressure as a function of density and total internal energy, and thus also as a function of $\boldsymbol{U}$: $p = p(\rho, E) = p(U_1, U_3 - \boldsymbol{U}_2^2/2U_1)$. For a calorically perfect gas, the expression is simply $p = (\gamma - 1)E = (\gamma - 1)(U_3 - \boldsymbol{U}_2^2/2U_1)$, where γ is the specific heat ratio. For real fluid equations of state, such a simple relation is not necessarily available. For instance, cubic equations of state express the pressure as a function of the temperature and specific volume, $p = p(T, v)$, but not as a function of the internal energy. In such cases, one can numerically compute the pressure, and thus flux $\boldsymbol{F}$, given the conservative variables and an equation of state.

Computation of the Riemann flux for a real fluid, $\hat{\boldsymbol{F}}$, needs further thoughts. In the present study, we consider a Roe-based approximate Riemann solver. Let $\boldsymbol{U}_L$ and $\boldsymbol{U}_R$ be the state variables on the boundaries of adjacent elements Ω_L and Ω_R. We define Roe's flux Jacobian $\tilde{\boldsymbol{A}}(= \boldsymbol{A}(\tilde{\boldsymbol{U}}))$ such that

$$\Delta \boldsymbol{F} = \tilde{\boldsymbol{A}} \Delta \boldsymbol{U}, \tag{2.17}$$

where $\tilde{(\cdot)}$ denotes the Roe-intermediate state and Δ is the difference operator: $\Delta(\cdot) = (\cdot)_R - (\cdot)_L$. The flux is then obtained through up-winding in terms of the Roe-intermediate state variables $\tilde{\boldsymbol{U}}$. The key to the Roe-scheme lies in determining $\tilde{\boldsymbol{A}}$, and thus $\tilde{\boldsymbol{U}}$, as functions of the left and right state variables $[\boldsymbol{U}_L, \boldsymbol{U}_R]$, such that the following mathematical conditions are satisfied: (1) $\Delta \boldsymbol{F} \to \boldsymbol{0}$ as $\Delta \boldsymbol{U} \to \boldsymbol{0}$, and (2) $\tilde{\boldsymbol{A}}$ is Hermitian.

For ideal gas, the following Roe-intermediate variables can be immediately computed

as

$$\tilde{\rho} = \sqrt{\rho_L \rho_R}, \tag{2.18}$$

$$\tilde{\boldsymbol{u}} = \frac{\sqrt{\rho_L}\boldsymbol{u}_L + \sqrt{\rho_R}\boldsymbol{u}_R}{\sqrt{\rho_L} + \sqrt{\rho_R}}, \tag{2.19}$$

$$\tilde{h^t} = \frac{\sqrt{\rho_L}h_L^t + \sqrt{\rho_R}h_R^t}{\sqrt{\rho_L} + \sqrt{\rho_R}}, \tag{2.20}$$

where h^t is the total specific enthalpy (Roe 1981). The Roe-intermediate speed of sound, which is required for up-winding the flux, is obtained as $\tilde{c} = (\gamma - 1)(\tilde{h}^t - \tilde{\boldsymbol{u}}^2/2)$.

For real fluid, however, equation (2.18) does not in general hold, and additional procedures are required to obtain $\tilde{\rho}$ and $\tilde{c}$. Such procedures have been established in FV methods for simulation of non-ideal gas dynamics (e.g., Glaister 1988; Vinokur & Montagné 1990). In this study, we adopt an approach introduced by Guardone (2007).

In the approach, we seek to find the Roe-intermediate density and the total energy that satisfy the following set of conditions

$$\begin{cases} \Delta p = \Delta\rho \left(\widetilde{\dfrac{\partial p}{\partial \rho}}\right)_E + \Delta E \left(\widetilde{\dfrac{\partial p}{\partial E}}\right)_\rho, & (2.21) \\ \tilde{h} = \tilde{h}^t - \dfrac{1}{2}\tilde{\boldsymbol{u}^2}. & (2.22) \end{cases}$$

The two equations correspond to the modified jump condition and consistency condition, respectively. For cubic equations of state, the analytic expression for p is given as a function of (T, v); thermodynamic variables, including the pressure derivatives and $\tilde{h}$, can be likewise analytically expressed using (T, v). In such cases, the above relations can be reduced to a multivariate function of $(\tilde{T}, \tilde{v})$, which can be solved numerically (Guardone 2007; Maeda *et al.* 2014). Once the Roe-intermediate variables are obtained, the intermediate speed of sound, that appears in the eigenvalue of $\tilde{\boldsymbol{A}}$, can be computed as

$$\tilde{c} = \sqrt{\left(\widetilde{\frac{\partial p}{\partial \rho}}\right)_E + \tilde{h}\left(\widetilde{\frac{\partial p}{\partial E}}\right)_\rho}. \tag{2.23}$$

Given the intermediate states and the speed of sound, computation of the Roe flux follows that of the standard Roe scheme. This Roe intermediate speed of sound can also be utilized in Harten-Lax-van Leer-contact (HLLC) -type approximate Riemann solvers (Rinaldi *et al.* 2014).

Finally, $\mathcal{D}$ is a function of the temperature derivatives with respect to the state variables, $\partial T/\partial \boldsymbol{U}$, which need to be computed. Similar to the pressure derivatives, an equation of state can be used to express temperature as a function of conservative variables: $T = T(\rho, E) = T(U_1, U_3 - \boldsymbol{U}_2^2/2U_1)$. To obtain $\partial T/\partial \boldsymbol{U}$, it then suffices to compute $(\partial T/\partial \rho)_E$ and $(\partial T/\partial E)_\rho$.

2.4. *Entropy bounding*

It is widely recognized that high-order DG methods can suffer from numerical instabilities in simulations that involve shock wave and the material's discontinuity (Shu 2016). An entropy-bounding technique, that was originally developed for time-dependent, nonlinear conservative difference equations (Tadmor 2003) has recently been found effective in enhancing robustness of a DG method without sacrificing high-order accuracy (Lv & Ihme

2015). The feasibility of this DG method, namely the entropy-bounded discontinuous-Galerkin (EBDG) method, was demonstrated through capturing strong shocks in calorically perfect gas. In the present study, we extend the technique to general equations of state to achieve a robust simulations of trans- and supercritical fluid flows.

We briefly review the entropy-bounding scheme for an ideal gas. For an ideal gas of a single substance, the entropy is expressed as

$$s = \log(p) - \gamma \log(\rho) + s_0, \tag{2.24}$$

where γ is a constant and s_0 is the entropy at a reference state. We define the entropy field in element Ω_e, which is spanned by the local basis functions. We consider states at times $t = t_0$ and $t_0 + \Delta t$, namely U_e^0 and $U_e^{\Delta t}$. Δt is chosen such that the Courant-Friedrich-Lax (CFL) condition is satisfied. Following the entropy principle, the bound for the entropy field at time $t = t_0 + \Delta t$ is defined as

$$\forall x \in \Omega_e, s(U_e^{\Delta t}(x)) \geq \min\{s(U(y))|y \in \Omega_e\} \equiv s_e^0(t). \tag{2.25}$$

The procedures for the entropy bounding scheme are as follows: (1) compute a local estimate for the entropy minimum in Ω_e that is consistent with the order of DG discretization: $|s_0^e(t) - \min\{s(\boldsymbol{U}(x))|\} \sim O(h^k)$, where k is the local order of accuracy; (2) apply a limiting operator L to the state $U_e^{\Delta t}(x)$ such that Eq. (2.25) is satisfied for the new state: $s({}^L\boldsymbol{U}_e^{\Delta t}) \geq s_e^0$.

The minimum entropy is estimated as

$$s_e^0(t) \approx \max\{M(s_e^0(t)), \min_{k \in N_e \bigcup \{e\}} s_k(t_0)\}, \tag{2.26}$$

where

$$\mathcal{M}(s_e^0(t)) = \min\{\min_{x \in D^-} s(\boldsymbol{U}(x)), s_m - \theta(s_n - s_m)\}. \tag{2.27}$$

s_m and s_n are the minimum and maximum entropy values in the element, respectively. θ is the relaxation factor and introduced to avoid overestimation

$$\theta = \frac{\min|x_m - x|}{|x_m - x_n|}, \tag{2.28}$$

where x_m and x_n denote the locations that provide s_m and s_n.

The mapping of the state by operator L is defined as

$${}^L\boldsymbol{U}_e = \boldsymbol{U}_e + \varepsilon(\overline{\boldsymbol{U}}_e - \boldsymbol{U}_e), \tag{2.29}$$

where ε is the limiting parameter, $\varepsilon \in [0, 1]$, and $\overline{\boldsymbol{U}}_e$ is the element-averaged state:

$$\overline{\boldsymbol{U}}_e = \frac{1}{V_e} \int_{\Omega_e} \boldsymbol{U}_e dv, \tag{2.30}$$

where V_e is the volume of element Ω_e. Using the expression for entropy, Eq. (2.24), Eq. (2.25) can be expressed as

$$p({}^L\boldsymbol{U}_e(\boldsymbol{x})) \geq \exp(s_e^0)\rho^\gamma({}^L\boldsymbol{U}_e(\boldsymbol{x})). \tag{2.31}$$

By substituting Eq. (2.29) and applying Jensen's inequality, we obtain

$$(1 - \varepsilon)p(\boldsymbol{U}_e) + \varepsilon p(\overline{\boldsymbol{U}}_e) \geq \exp(s_e^0)[(1 - \varepsilon)\rho^\gamma(\boldsymbol{U}_e) + \varepsilon\rho^\gamma(\overline{\boldsymbol{U}}_e)], \tag{2.32}$$

where ε is readily evaluated as

$$\varepsilon = \frac{\tau}{\tau - [p(\overline{\boldsymbol{U}}_e) - \exp(s_e^0)\rho^\gamma(\boldsymbol{U}_e)]}, \tag{2.33}$$

with

$$\tau = \min\{0, \min\{p(\boldsymbol{U}_e) - \exp(s_e^0)\rho^\gamma(\boldsymbol{U}_e)\}\}. \tag{2.34}$$

We note that the positivity of the density, $\rho({}^L\boldsymbol{U}_e) > 0$, is satisfied through the above procedure.

To extend the entropy-bounding scheme to a real fluid, we consider two modifications. First, we relax the definition of entropy:

$$s = \log(p) - \gamma^* \log(\rho) + s_0, \tag{2.35}$$

where γ^* is now a function of thermodynamic state variables. During the simulation, γ^* is dynamically computed using the following thermodynamic definition of the speed of sound

$$\gamma* = \frac{\rho c^2}{p} = \frac{\rho}{p}\left[\left(\frac{\partial p}{\partial \rho}\right)_E + h\left(\frac{\partial p}{\partial E}\right)_\rho\right]. \tag{2.36}$$

The expression for entropy using γ^* is convenient since the above entropy principle and the limiting operator L can be directly adopted by replacing γ with γ^*.

Second, we introduce an additional bound for the density: $\rho < 1/b$, where b is the co-volume. The co-volume is an effective volume of the molecules in a condensed state of liquid. The physical meaning of this inequality is that the volume of fluid cannot be smaller than the total volume of molecules. For cubic equations of state, the co-volume is defined as a function of the critical temperature and the critical pressure. Note that the co-volume is defined zero for ideal fluid.

3. Result

3.1. *Density wave of transcritical nitrogen*

The first test case is a density wave of transcritical nitrogen. This case is designated to assess the accuracy of the present DG method in simulating the dynamics of transcritical fluids whose state change across the pseudo-boiling line. A similar case was considered by Kawai *et al.* (2015) using their FD approach. We consider a one-dimensional, periodic computational domain defined as $x \in [-l/2, l/2]$, where $l = 1.0$ m. Nitrogen with a sinusoidal density profile and uniform pressure is advected with a constant velocity in the domain. The initial condition is defined as

$$\rho = \rho_{cr}[1 + 0.8\sin(2\pi x)], \tag{3.1}$$

$$u = u_0, \tag{3.2}$$

$$p = 1.03 p_{cr}, \tag{3.3}$$

where ρ_{cr} and p_{cr} are the critical density and the critical pressure, and $u_0 = 100$ m s^{-1}. Both the density and temperature vary across their critical values, while the pressure is maintained slightly above the critical pressure. The domain is uniformly discretized using various values of elements within a range of $N_e \in [10, 80]$. We advance the solution during a single period of advection up to $t = l/u_0$, using the DG scheme with polynomial orders of $p = 1$ (DG-$p1$) and $p = 2$ (DG-$p2$). For all simulations, the strong stability preserving third-order Runge-Kutta (SSPRK3) scheme (Gottlieb *et al.* 2001) is employed for time marching the solution with a constant CFL number of $C = 0.1$. The diffusive flux is set to zero.

Figure 1 shows the density and velocity fields obtained from the simulations at $t = l/u_0$

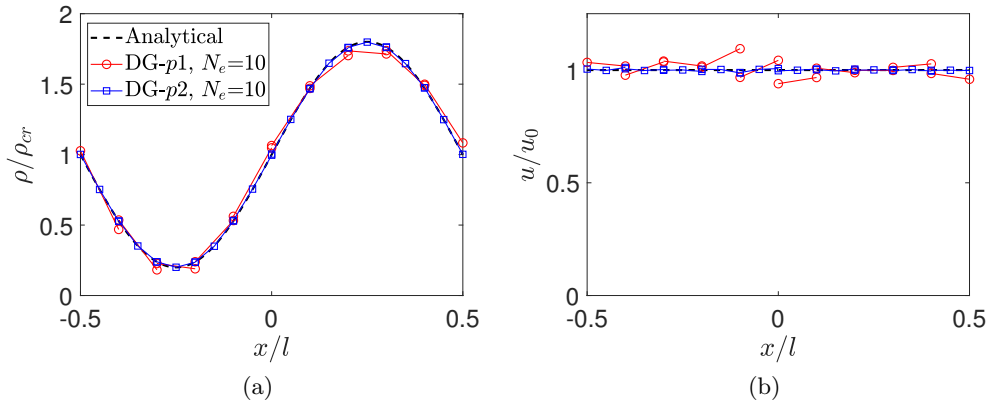

(a) (b)

Figure 1: Solutions at $t = l/u_0$ s obtained using DG-$p1$ and DG-$p2$. $N_e = 10$ for both cases. (a) Density and (b) Velocity are shown.

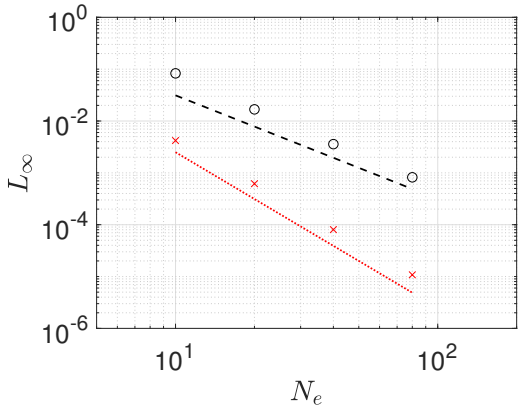

Figure 2: L_∞ error norm of the density at $t = l/u_0$ s obtained using (○) DG-$p1$ and (×) DG-$p2$. Slopes corresponding to second- and third-order convergence are shown for reference.

using DG-$p1$ and DG-$p2$ with $N_e = 10$, respectively. Deviations from the analytical solution are smaller with DG-$p2$, highlighting the advantage of high-order polynomial to better approximate the solution.

In order to quantify the error and validate the accuracy of the scheme, we perform convergence tests using the results of the simulations. Figure 2 shows the L_∞ norm of the density as a function of the number of elements. The plot indicates that optimal convergence is achieved for both DG-$p1$ and DG-$p2$. With the same values of N_e, the error is smaller with DG-$p2$ than with DG-$p1$, highlighting the improvement of accuracy by using high-order polynomials. Entropy-bounding is not required to obtain the stable solution.

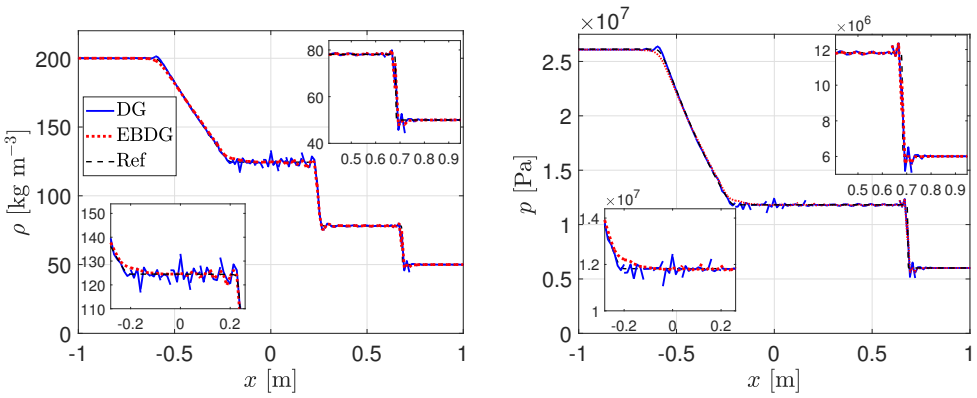

(a) (b)

Figure 3: Solutions of the shock tube problem at $t = 1.2 \times 10^{-2}$ s obtained using DG-$p3$ and EBDG-$p3$. $N_e = 50$ in both cases. (a) Density and (b) pressure are shown.

3.2. *Supercritical shock tube problem*

In order to assess the performance of the EBDG method in capturing discontinuities in supercritical fluids, we simulate a shock tube problem of supercritical nitrogen. We consider a one-dimensional, non-periodic domain defined as $x \in [-1, 1]$ m. The initial condition is defined as

$$(\rho, u, T) = \begin{cases} (200, 0, 400), & -1 \leq x < 0 \ \text{m}. \\ (50, 0, 400), & 0 \leq x \leq 1 \ \text{m}, \end{cases} \tag{3.4}$$

where T is the temperature. The units for (ρ, u, T) are kg m^{-3}, m s^{-1}, and K, respectively. We use DG-$p3$ and EBDG-$p3$ to obtain solutions with $N_e = 50$, and compare results. SSPRK3 is employed for time marching the solution with a constant CFL number of $C = 0.1$. The diffusive flux is set to zero.

Figure 3 shows the density and pressure fields at $t = 1.2 \times 10^{-3}$ s. In both plots, the DG solutions present significant oscillations in regions between the rarefaction wave and the contact discontinuity, and near the shock. The EBDG solutions are smoother in the entire domain. Although the oscillations are not completely removed, they are localized near discontinuities and their amplitudes are reduced compared to the DG solutions. The results indicate that the present EBDG method is effective in capturing discontinuities in supercritical flows.

The oscillations observed in the EBDG solution are not expected to immediately cause divergence of the solution (code blow up) since the entropy principle is satisfied. Numerical oscillations near discontinuities in EBDG solutions were previously observed in shock capturing of a calorically perfect gas (Lv & Ihme 2015).

In the present test case, when further smoothness is desirable in the solution, we find AV effective in removing the oscillations. Figure 4 shows the solutions of the shock tube problem obtained using EBDG-$p3$ and EBDG-$p3$ with AV. The same physical parameters are used as in the previous cases. The solutions show that AV removes oscillations without a noticeable increase in the thickness of the regions of discontinuities.

The results of the test cases in the previous and the present sections indicate that the entropy-bounding scheme may not be required to achieve designated high-order accuracy,

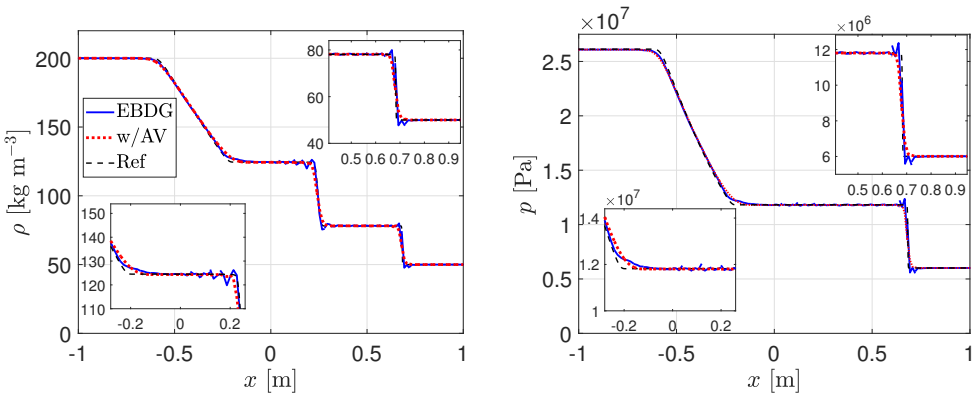

Figure 4: Solutions of the shock tube problem at $t = 1.2 \times 10^{-2}$ s obtained using EBDG-$p3$ and EBDG-$p3$ with AV. $N_e = 50$ in both cases. (a) Density and (b) pressure are shown.

while the scheme can be essential in simulations of flows with discontinuities. In practical direct numerical simulation of trans- and supercritical fluid flows, physical diffusivity may stabilize the simulation without additional numerical stabilization. For under-resolved simulations of turbulent flows that requires modeling of dissipation at the sub-grid-scale, the entropy-bounding scheme can be a means to inject numerical diffusion and implicitly stabilize the simulation (Moura *et al.* 2017; Lv *et al.* 2018). The present formulation of the DG and EBDG methods can also include sub-grid scale modeling for explicit large-eddy simulations.

3.3. *Density stratified shear layer of transcritical nitrogen*

The last test case is a density stratified, temporally evolving, counter-flow shear layer of transcritical nitrogen. This case models the surface of a liquid jet during cryogenic nitrogen injection (Oschwald *et al.* 2006). We consider a two-dimensional computational domain in x-y Cartesian coordinates: $x \in [-0.5, 0.5], y \in [-0.25, 0.25]$ m. The initial condition is defined as

$$\rho = \rho_{cr}(1 + \Delta \tanh(ay)), \tag{3.5}$$

$$u = u_0(1 + \Delta \tanh(ay)), \tag{3.6}$$

$$v = 0, \tag{3.7}$$

$$p = 1.47 p_{cr}, \tag{3.8}$$

where $u_0 = 40$ m s^{-1}, $\Delta = 0.2$, and $a = 40$. Small-amplitude perturbations are added to the velocity field to trigger the Kelvin–Helmholtz instability (Sharan *et al.* 2019). Similar to the density wave case, the fluid is in a pseudo-boiling condition; both density and temperature vary from subcritical to supercritical values across the layers. The domain is uniformly discretized by 200×100 elements. Periodic boundary conditions are used in the domain boundaries along the x-axis, while symmetry boundary conditions are used in those along the y-axis. The Navier-Stokes equation is solved with the diffusive flux obtained using the BR2 scheme (Bassi & Rebay 1997). DG-$p5$ and SSPRK3 are used for spatial discretization and time marching, respectively.

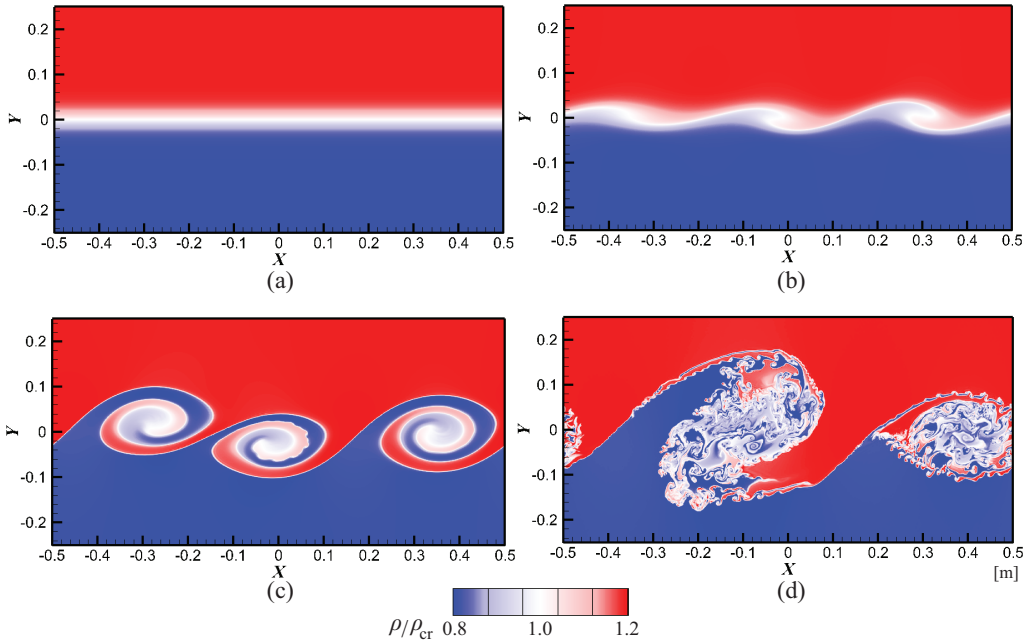

Figure 5: Contours of the density field at (a) $t = 0$, (b) 4.0×10^{-2}, (c) 5.2×10^{-2}, and (d) 6.0×10^{-2} s.

Figure 5 shows the evolution of the density contours obtained in the simulation. Spanwise KelvinHelmholtz rollers are developed and amalgamate. Although the simulation is two-dimensional, turbulence-like, small-scale structures are observed in the rollers in Figure 5d. The evolution of such structures can enhance the mixing of the layers.

Figure 6 shows scatter plots of pressure as a function of density in the flow field at instances corresponding to the contours in Figures 5. The range of distribution of the scatter points steadily spreads in both pressure and density. This spread may clearly be due to the growth of the Kelvin–Helmholtz rollers that result in enhancement of the fluctuations in the fluid. Scatter points in all plots are placed above the critical pressure and span the critical density, indicating that the fluid in the mixing region is in pseudo-boiling conditions at all instances. Overall, the results highlight the capability of the present DG-method in simulating the multi-dimensional dynamics of compressible transcritical fluid flows in a pseudo-boiling regime.

4. Conclusions

In this study, we developed a high-order DG method that is capable of simulating trans- and supercritical fluid flows. A Riemann solver that accounts for real fluid thermodynamics was combined with a DG framework that solves the conservative form of the compressible Navier-Stokes equations. An entropy-bounding strategy was introduced to enhance the robustness of the method in capturing discontinuities. Validation and demonstration of the method were described through simulations of a density wave, a shock tube problem, and a shear layer of trans- and supercritical nitrogen. To the best of our knowledge, this study presents the first DG simulation of pseudo-boiling fluid flows.

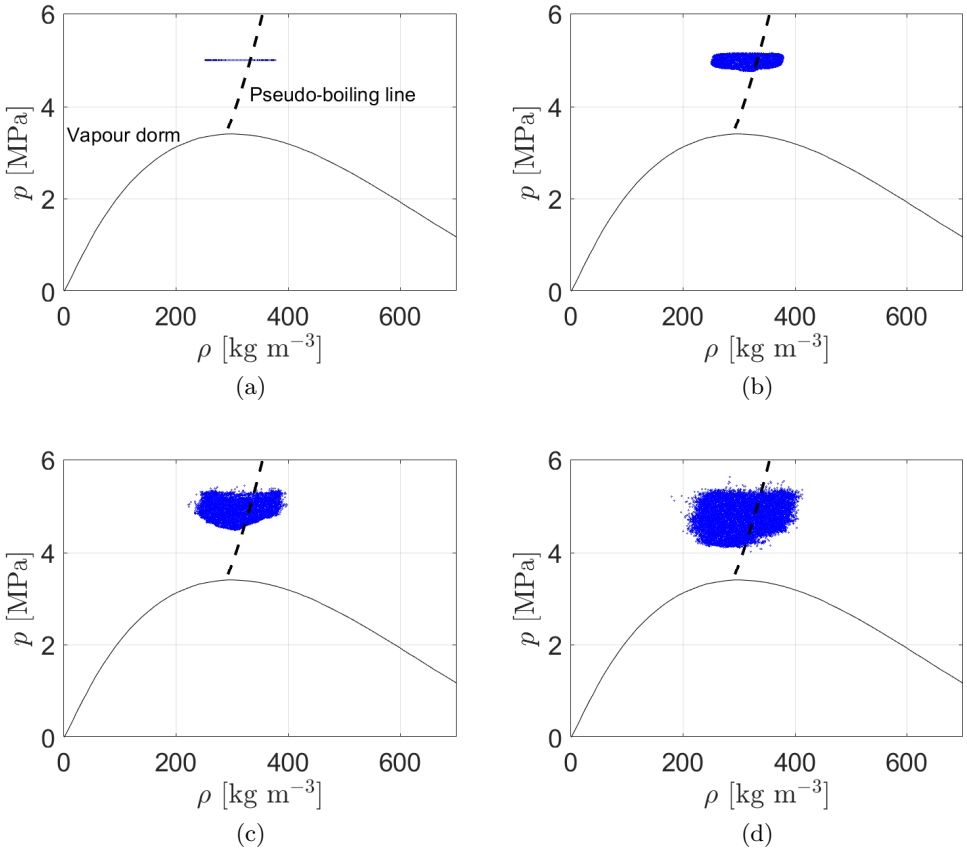

Figure 6: Scatter plots of pressure as a function of density in the flow field at (a) $t = 0$, (b) 4.0×10^{-2}, (c) 5.2×10^{-2}, and (d) 6.4×10^{-2} s. Solid line and dashed line denote vapor-liquid saturation curve (vapor dorm) and pseudo-boiling line, respectively.

The method can be of use for simulations of various regimes of non-ideal gas dynamics and trans- and super-critical flows that may require high-order accuracy, modeling of complex geometries, and/or efficient parallelization. Future work will include simulation and analysis of three-dimensional, turbulent trans- and supercritical fluid flows.

Acknowledgments

This investigation was supported through NASA. Helpful discussions with Kihiro Bando, Steven Brill, and Eric Ching are acknowledged.

REFERENCES

Banuti, D., Raju, M., Ma, P. C., Ihme, M. & Hickey, J.-P. 2017 Seven questions about supercritical fluids-towards a new fluid state diagram. In *55th AIAA Aerospace Sciences Meeting*, p. 1106.

Bassi, F. & Rebay, S. 1997 High-order accurate discontinuous finite element solution of the 2D Euler equations. *J. Comput. Phys.* **138**, 251–285.

Billet, G. & Abgrall, R. 2003 An adaptive shock-capturing algorithm for solving unsteady reactive flows. *Comput. Fluids* **32**, 1473–1495.

Ching, E. J., Lv, Y., Gnoffo, P., Barnhardt, M. & Ihme, M. 2019 Shock capturing for discontinuous Galerkin methods with application to predicting heat transfer in hypersonic flows. *J. Comput. Phys.* **376**, 54–75.

Cockburn, B. & Shu, C.-W. 1998 The local discontinuous Galerkin method for time-dependent convection-diffusion systems. *SIAM J. Numer. Anal.* **35**, 2440–2463.

Fidkowski, K. J. 2004 A high-order discontinuous Galerkin multigrid solver for aerodynamic applications. PhD thesis, Massachusetts Institute of Technology.

Föll, F., Pandey, S., Chu, X., Munz, C.-D., Laurien, E. & Weigand, B. 2019 High-fidelity direct numerical simulation of supercritical channel flow using discontinuous Galerkin spectral element method. In *High Performance Computing in Science and Engineering'18*, pp. 275–289. Springer.

de Frahan, M. T. H., Varadan, S. & Johnsen, E. 2015 A new limiting procedure for discontinuous Galerkin methods applied to compressible multiphase flows with shocks and interfaces. *J. Comput. Phys.* **280**, 489–509.

Glaister, P. 1988 An approximate linearised Riemann solver for the euler equations for real gases. *J. Comput. Phys.* **74**, 382–408.

Gottlieb, S., Shu, C.-W. & Tadmor, E. 2001 Strong stability-preserving high-order time discretization methods. *SIAM Rev.* **43**, 89–112.

Guardone, A. 2007 Three-dimensional shock tube flows for dense gases. *J. Fluid Mech.* **583**, 423–442.

Kawai, S., Terashima, H. & Negishi, H. 2015 A robust and accurate numerical method for transcritical turbulent flows at supercritical pressure with an arbitrary equation of state. *J. Comput. Phys.* **300**, 116–135.

Kim, K., Hickey, J.-P. & Scalo, C. 2019 Pseudophase change effects in turbulent channel flow under transcritical temperature conditions. *J. Fluid Mech.* **871**, 52–91.

Knez, Ž., Markočič, E., Leitgeb, M., Primožič, M., Hrnčič, M. K. & Škerget, M. 2014 Industrial applications of supercritical fluids: A review. *Energy* **77**, 235–243.

Lv, Y. & Ihme, M. 2015 Entropy-bounded discontinuous Galerkin scheme for Euler equations. *J. Comput. Phys.* **295**, 715–739.

Lv, Y., Ma, P. C. & Ihme, M. 2018 On underresolved simulations of compressible turbulence using an entropy-bounded DG method: solution stabilization, scheme optimization, and benchmark against a finite-volume solver. *Comput. Fluids* **161**, 89–106.

Lv, Y., See, Y. C. & Ihme, M. 2016 An entropy-residual shock detector for solving conservation laws using high-order discontinuous Galerkin methods. *J. Comput. Phys.* **322**, 448–472.

Ma, P. C., Lv, Y. & Ihme, M. 2017 An entropy-stable hybrid scheme for simulations of transcritical real-fluid flows. *J. Comput. Phys.* **340**, 330–357.

Maeda, K., Blanquart, G. & Colonius, T. 2014 Internal report for Energent project. *Tech. Rep.*. California Institute of Technology.

Mengaldo, G. 2015 Discontinuous spectral/hp element methods: development, analysis and applications to compressible flows. PhD thesis, Imperial College London.

e.g. Miller, R. S., Harstad, K. G. & Bellan, J. 2001 Direct numerical simulations

of supercritical fluid mixing layers applied to heptane–nitrogen. *J. Fluid Mech.* **436**, 1–39.

Moura, R. C., Mengaldo, G., Peiró, J. & Sherwin, S. J. 2017 On the eddy-resolving capability of high-order discontinuous Galerkin approaches to implicit LES/under-resolved dns of euler turbulence. *J. Comput. Phys.* **330**, 615–623.

Oschwald, M., Smith, J., Branam, R., Hussong, J., Schik, A., Chehroudi, B. & Talley, D. 2006 Injection of fluids into supercritical environments. *Combust. Sci. Technol.* **178**, 49–100.

Pantano, C., Saurel, R. & Schmitt, T. 2017 An oscillation free shock-capturing method for compressible Van der Waals supercritical fluid flows. *J. Comput. Phys.* **335**, 780–811.

Persson, P.-O. & Peraire, J. 2006 Sub-cell shock capturing for discontinuous Galerkin methods. In *44th AIAA Aerospace Sciences Meeting and Exhibit*, p. 112.

Rinaldi, E., Pecnik, R. & Colonna, P. 2014 Exact Jacobians for implicit Navier–Stokes simulations of equilibrium real gas flows. *J. Comput. Phys.* **270**, 459–477.

Robinson, D. B., Peng, D.-Y. & Chung, S. Y. 1985 The development of the Peng–Robinson equation and its application to phase equilibrium in a system containing methanol. *Fluid Ph. Equilibria* **24**, 25–41.

Roe, P. L. 1981 Approximate Riemann solvers, parameter vectors, and difference schemes. *J. Comput. Phys.* **43**, 357–372.

Sharan, N., Matheou, G. & Dimotakis, P. E. 2019 Turbulent shear-layer mixing: initial conditions, and direct-numerical and large-eddy simulations. *J. Fluid Mech.* **877**, 35–81.

Shu, C.-W. 2016 High order WENO and DG methods for time-dependent convection-dominated PDEs: A brief survey of several recent developments. *J. Comput. Phys.* **316**, 598–613.

Tadmor, E. 2003 Entropy stability theory for difference approximations of nonlinear conservation laws and related time-dependent problems. *Acta Numer.* **12**, 451–512.

Terashima, H. & Koshi, M. 2012 Approach for simulating gas–liquid-like flows under supercritical pressures using a high-order central differencing scheme. *J. Comput. Phys.* **231**, 6907–6923.

Vinokur, M. & Montagné, J.-L. 1990 Generalized flux-vector splitting and Roe average for an equilibrium real gas. *J. Comput. Phys.* **89**, 276–300.